

NASA Technical Memorandum 104606, Vol. 10

**Technical Report Series on
Global Modeling and Data Assimilation**

Max J. Suarez, Editor
*Goddard Space Flight Center
Greenbelt, Maryland*

Volume 10

**Dynamical Aspects of Climate
Simulations Using the GEOS General
Circulation Model**

Lawrence L. Takacs
General Sciences Corporation, Laurel, Maryland

Max J. Suarez
Goddard Space Flight Center, Greenbelt, Maryland



Goddard Space Flight Center
Greenbelt, Maryland
March 1996

Abstract

The general circulation simulated by Version 1 of the Goddard Earth Observing System (GEOS-1) general circulation model is compared with the five-year reanalysis recently completed using the GEOS-1 data assimilation system. Emphasis is on the comparison of dynamical quantities, such as heat and momentum fluxes. The results indicate that, while many features are well simulated, the model exhibits a number of severe biases. These include: a cold bias at both poles and an associated westerly bias at upper levels, a strong low-level westerly bias during northern hemisphere winter, a dry tropical boundary layer and excessive moisture at all levels outside the tropics, too much poleward heat and momentum flux by transient eddies, and too little heat flux by stationary eddies.

The effects on these biases of increasing resolution and order of accuracy, of including a parameterization of gravity wave drag, and of increasing the vertical extent of the model are also examined. The main impacts of increasing resolution and accuracy are found to be on the transient eddy statistics. The higher-order and higher-resolution experiments are in closer agreement with observations in the southern hemisphere, where the fluxes are primarily determined by the transient flow; however, in the northern hemisphere, where the fluxes due to the stationary flow are important, the more “accurate” simulations are systematically further from the analysis. As in several other studies, gravity wave drag is found to have a beneficial effect on both the time-mean flow and the transient statistics in the northern hemisphere, while little impact is seen in the southern hemisphere. Increasing the vertical extent of the model significantly improves the cold pole and westerly bias in the southern hemisphere.

Contents

List of Figures	vii
List of Tables	ix
1 Introduction	1
2 Model Description	2
2.1 GEOS GCM	2
2.2 GEOS DAS	3
3 Comparison of GEOS-1 Simulation and Analysis	5
3.1 The Zonal Mean Circulation	5
3.2 The Stationary Flow	8
3.3 Eddy Statistics	9
4 Resolution and Order-of-Accuracy Studies	10
4.1 The Zonal Mean Circulation	11
4.2 Eddy Statistics	13
5 The Effects of Gravity Wave Drag	15
6 Summary	19

List of Figures

1	Five year average of Northern Hemisphere winter zonal mean u-winds (m sec^{-1}) for the GEOS-1 GCM, the GEOS-1 DAS, and the u-wind and temperature difference (GCM-DAS).	25
2	Five year average of Northern Hemisphere summer zonal mean u-winds (m sec^{-1}) for the GEOS-1 GCM, the GEOS-1 DAS, and the u-wind and temperature difference (GCM-DAS).	26
3	Five year average of Northern Hemisphere winter and summer seasonal means of the zonal mean v-wind (m sec^{-1}) for the GEOS-1 GCM, the GEOS-1 DAS, and the uninitialized ECMWF analysis.	27
4	Five year average of JJA seasonal mean of the zonal mean a) specific humidity (g kg^{-1}) for the GEOS-1 GCM, b) specific humidity difference for the GCM-DAS, c) specific humidity difference due to temperature, d) specific humidity difference due to relative humidity, e) blended relative humidity using GEOS-1 DAS and SAGE, f) relative humidity from the GEOS-1 GCM.	28
5	Five year average of Northern Hemisphere winter seasonal means of the 200-mb u-wind (5 m sec^{-1}) contours, with negatives shaded) and 300-mb eddy-heights (60 m contours, with light shading $< 60 \text{ m}$ and dark shading $> 60 \text{ m}$) for the GEOS-1 GCM and the GEOS-1 DAS.	29
6	Five year average of Northern Hemisphere winter and summer seasonal means of Sea-Level Pressure (4 mb contours, with light shading $< 988 \text{ mb}$ and dark shading $> 1020 \text{ mb}$) for the GEOS-1 GCM and the GEOS-1 DAS.	30
7	Five year average of DJF seasonal mean of the eddy Sea-Level Pressure (4 mb contours, with light shading $< -4 \text{ mb}$ and dark shading $> 4 \text{ mb}$) for the GEOS-1 GCM and the GEOS-1 DAS.	31
8	Five year average of DJF and JJA seasonal means of the vertically integrated momentum flux ($\text{m}^2 \text{ sec}^{-2}$), and kinetic energy ($\text{m}^2 \text{ sec}^{-2}$), due to the transient and stationary flow for the GEOS-1 GCM and the GEOS-1 DAS.	32
9	Five year annual mean average of horizontal momentum flux ($\text{m}^2 \text{ sec}^{-2}$) and kinetic energy ($\text{m}^2 \text{ sec}^{-2}$) due to the transient flow for the GEOS-1 GCM and the GEOS-1 DAS.	33
10	Five year annual mean average of horizontal momentum flux ($\text{m}^2 \text{ sec}^{-2}$) and kinetic energy ($\text{m}^2 \text{ sec}^{-2}$) due to the stationary flow for the GEOS-1 GCM and the GEOS-1 DAS.	34

11	Five year average of DJF and JJA seasonal means of the vertically integrated heat ($\text{m sec}^{-1} \text{ deg}$), and moisture ($\text{m sec}^{-1} \text{ g kg}^{-1}$) fluxes due to the transient and stationary flow for the GEOS-1 GCM and the GEOS-1 DAS.	35
12	Five year annual mean average of meridional heat flux ($\text{m sec}^{-1} \text{ deg}$) due to the transient and stationary flow for the GEOS-1 GCM and the GEOS-1 DAS.	36
13	Five year annual mean average of meridional moisture flux ($\text{m sec}^{-1} \text{ g kg}^{-1}$) due to the transient and stationary flow for the GEOS-1 GCM and the GEOS-1 DAS.	37
14	Two year annual and zonal mean u-wind (m sec^{-1}) in the southern hemisphere for the Control (H22) run, experiments L22, L42, L44, H44, and the GEOS-1 DAS.	38
15	Two year annual and zonal mean u-wind (m sec^{-1}) in the northern hemisphere for the Control (H22) run, experiments L22, L42, L44, H44, and the GEOS-1 DAS.	39
16	Two year annual and zonal mean temperature (deg K) at 100 mb for the Control (H22) run, experiments L22, L42, L44, H44, and the GEOS-1 DAS.	40
17	Two year annual and zonal mean differences in precipitable water (g cm^{-2}) between a) experiments L22 through H44 and the Control (H22), and b) between L22 through H44, the Control (H22), and the GEOS-1 DAS.	41
18	Vertically integrated poleward momentum flux for the Control (H22) run, experiments L22, L42, L44, H44, and the GEOS-1 DAS, due to transient and stationary flow.	42
19	Vertically integrated poleward heat flux for the Control (H22) run, experiments L22, L42, L44, H44, and the GEOS-1 DAS, due to transient and stationary flow.	43
20	Vertically integrated poleward moisture flux for the Control (H22) run, experiments L22, L42, L44, H44, and the GEOS-1 DAS, due to transient and stationary flow.	44
21	Five year Northern Hemisphere winter seasonal averages of momentum torques for (a) the GEOS-1 DAS, and (b) the GEOS-1 GCM. Also shown is the two year DJF seasonal average for (c) the GEOS GCM with Gravity Wave Drag (L44 w/GWD). (Units are in 10^6 N m^{-1})	45
22	Two year DJF seasonal mean difference of momentum torques from the GEOS GCM with Gravity Wave Drag (L44 w/GWD) and the control (L44). (Units are in 10^6 N m^{-1})	46

23	Vertically integrated annual mean momentum and heat flux due to transient and stationary flow for the GEOS-1 DAS and experiments L44 and L44 w/GWD.	47
24	DJF Seasonal mean Sea-Level Pressure and 300 mb Eddy Heights from the GEOS GCM w/GWD and the GEOS-1 DAS.	48
25	Two year average of DJF zonal mean u-winds (m sec^{-1}) for the GEOS GCM w/GWD and the Stratospheric GEOS GCM w/GWD, and their temperature differences (GCM-DAS).	49
26	Stencil showing the position and indexing of the prognostic fields u , v , and h , together with the vorticity, ζ , and the scheme parameters α , β , γ , δ , ν , and μ	50

List of Tables

1	GEOS-1 Sigma Level Distribution	4
2	Sensitivity Experiments Summary	11

1 Introduction

The GEOS general circulation model (GCM) is part of the data assimilation system (DAS) being developed at Goddard's Data Assimilation Office (DAO) for use by NASA's Earth Observing System program. The primary objective of this system is to produce research quality datasets from the satellite and surface measurements of the earth system that will be available at the turn of the century.

Although both the model and the analysis algorithms are still under development, a preliminary version of the DAS (the GEOS-1 DAS) has already been used in a number of applications. Perhaps the most important and visible of these has been the production of a global reanalysis of atmospheric data (Schubert et al. 1993 and Schubert et al. 1995), which is now generally available to the atmospheric research community. This version of the DAS has also been used for shorter assimilations in support of the Coupled Ocean-Atmosphere Response Experiment (COARE), of subprojects of the Global Energy and Water Cycle Experiment (GEWEX), and of the Airborne Southern Hemisphere Ozone Experiment (ASHOE) mission. In addition to these data assimilation applications, the GEOS GCM is also being used for climate simulations, and results from a low-resolution version of the model have been submitted to the Atmospheric Model Intercomparison Project (AMIP) (Gates, 1992).

Because of the wide dissemination of these results, particularly of the data assimilation products, we felt it was important that the behavior of the atmospheric GCM used to produce them be thoroughly documented. The behavior of physical processes in the model, such as moist convection, radiative heating, surface fluxes, and the hydrological cycle are the focus of Molod et al. (1996).

In this paper we concentrate on the behavior of the model's circulation statistics, emphasizing those biases in the simulated climate that may affect the analysis through systematic errors in the model provided first guess. This information is necessary both for a critical evaluation of the analysis products and to identify model deficiencies that need to be addressed in future versions of the system. A second purpose of the paper is to preview the effects of some of the modifications to the model that will be included in future versions of the system and to begin to assess the impact of increasing horizontal resolution.

In section 3 we compare the climatology of a five-year simulation with that of the five-year GEOS-1 DAS reanalysis. An extensive comparison is made of both primary fields (wind, temperature, moisture, and pressure) and second moments (transient and stationary momentum, heat, and moisture fluxes). We believe that this is the first time in which long-term climatologies from a simulation and an unchanging data assimilation system using the same general circulation model have been directly compared.

In section 4 we examine the sensitivity of the GEOS GCM to horizontal resolution and order-of-accuracy. A number of studies have considered the impact of increasing horizontal resolution (for example, Mahlman and Umscheid (1987), Boer and Lazare (1988),

Tibaldi et al. (1990), Boville (1991), and Boyle (1993)). As mentioned in Boyle (1993), the rationale for these studies is to determine the coarsest (and presumably most efficient) resolution which adequately simulates the atmospheric climate signal in question. The impact of order-of-accuracy within dynamical systems has also been examined by several investigators. Kreiss and Olinger (1972) were among the first to discuss the merits of using higher-order accuracy to reduce space truncation errors and improve the phase characteristics of wave propagation. Other examples include Kalnay-Rivas et al. (1976), in which the impact of fourth-order over second-order accuracy in short-range weather prediction was examined, and Russell et al. (1986) who compared the ability of several shallow water numerical schemes of second- and fourth-order to simulate a Rossby-Haurwitz wave. While the advantages of higher-order accuracy for passive tracer advection and short-range forecasting are readily apparent from the studies just cited, the climatological response of a GCM to such changes has not received similar attention. In this study we examine the impact of order-of-accuracy on the climatology produced from long-term GCM simulations, and compare them to both the GEOS-1 GCM benchmark and the GEOS-1 DAS analysis. For this sensitivity study, the GEOS GCM was run using two horizontal resolutions ($4^\circ \times 5^\circ$ and $2^\circ \times 2.5^\circ$) and two higher-order versions being evaluated for implementation in the DAS.

In section 5, we present results from a version of the model that includes the gravity wave drag parameterization of Alpert et al. (1988), as modified by Zhou et al. (1996). As has been noted many times since the studies of Palmer et al. (1986) and McFarlane (1987), the inclusion of gravity wave drag in the troposphere and lower stratosphere can have a strong impact on the zonal mean circulation, the stationary wave pattern, and even on the model's transient statistics. We find all of these impacts to occur, and in nearly all cases to have a strongly beneficial effect on many of the most egregious biases noted in the GEOS-1 simulation. We conclude section 5 with an examination of the impact of increasing the vertical extent of the model by including a well-resolved stratosphere up to 0.1 mb.

We begin, in section 2, with a brief description of the GEOS-1 GCM and the GEOS-1 DAS.

2 Model Description

2.1 GEOS GCM

We describe first the GEOS-1 GCM, which is the version of the model that was used in the GEOS-1 reanalysis, and which will be the focus of much of our attention and serve as a baseline or "Control" for our sensitivity studies.

The GEOS-1 GCM uses the second-order version of the Aries/GEOS dynamical core described in Suarez and Takacs (1995). This core is a modular, Eulerian, finite-difference dynamics package used for many global modeling applications at Goddard. The equations are finite-differenced on an Arakawa C-grid in the horizontal and a Lorenz grid on a standard

σ coordinate in the vertical. The horizontal finite-differencing of the momentum equation is based on the second-order energy and potential enstrophy conserving scheme of Sadourny, as described in Burridge and Haseler (1977). In the thermodynamic and moisture equations the horizontal differencing is based on the standard, square-conserving, second-order scheme. The vertical finite differencing is that of Arakawa and Suarez (1983).

The physics package includes a full set of sub-grid parameterizations. Penetrative and shallow cumulus convection are parameterized using the Relaxed Arakawa-Schubert scheme of Moorthi and Suarez (1992), coupled with a Kessler-type scheme for the re-evaporation of falling rain (Sud and Molod, 1988). The thermal and solar radiation parameterizations follow closely those described by Harshvardhan et al. (1987). Cloudiness is diagnosed using a simple scheme based on the incidence of cumulus convection and large-scale condensation. Turbulent eddy fluxes of momentum, heat, and moisture in the surface layer are calculated using stability-dependent bulk formulas based on Monin-Obukhov similarity functions. Above the surface layer, turbulent fluxes of momentum, heat, and moisture are calculated by the Level 2.5 Mellor-Yamada type closure scheme of Helfand and Labraga (1988), which predicts turbulent kinetic energy and determines the eddy transfer coefficients used for a bulk formulation. The GEOS-1 GCM does not include a parameterization of gravity-wave drag. For a more complete description of the model, refer to Takacs et al. (1994).

The GEOS-1 five-year simulation presented in section 3 and the corresponding GEOS-1 DAS five-year reanalysis were run using the same horizontal ($2^\circ \times 2.5^\circ$) and vertical (20 layers) resolution. The vertical distribution of the sigma levels is given in Table 1; these are chosen so as to provide enhanced resolution in the planetary boundary layer and near the tropopause. The top of the model atmosphere is at 10 mb, where we assume $\dot{\sigma} = 0$.

2.2 GEOS DAS

As previously mentioned, we will compare the simulations with the DAO's five-year reanalysis of March 1985 through February 1990. The data assimilation system used for this reanalysis (the GEOS-1 DAS) is described in detail in Pfaendtner et al. (1995). An overview of the results is presented in Schubert et al. (1995). The GEOS-1 DAS employs the GEOS-1 GCM in conjunction with an Optimal Interpolation (OI) analysis scheme (based on Baker et al. 1987) and the Incremental Analysis Updating (IAU) proposed by Bloom et al. (1996) and Bloom et al. (1991).

The OI is a three-dimensional (multivariate in z, u, v ; univariate in mixing ratio), statistical objective analysis scheme employing damped cosine horizontal autocorrelation functions for model prediction error, and a multivariate oceanic surface analysis incorporating an Ekman balance for the sea-level pressure and winds. Observational data for the surface analysis consists of surface land, ship, and buoy reports. The upper-air analysis incorporates data from rawinsondes, dropwindsondes, rocketsondes, aircraft winds, cloud tracked winds, and thicknesses from the Tiros Operational Vertical Sounder (TOVS).

Table 1: GEOS-1 Sigma Level Distribution

Level	Sigma	Δ Sigma
1	0.009500	0.019000
2	0.029000	0.020000
3	0.049750	0.021500
4	0.073000	0.025000
5	0.100050	0.029100
6	0.132200	0.035200
7	0.172150	0.044700
8	0.222750	0.056500
9	0.283750	0.065500
10	0.352000	0.071000
11	0.424750	0.074500
12	0.500500	0.077000
13	0.578390	0.078779
14	0.657113	0.078669
15	0.734480	0.076064
16	0.807832	0.070641
17	0.874136	0.061967
18	0.929925	0.049610
19	0.971300	0.033141
20	0.993935	0.012129

The OI is performed every 6 hours using observations from a ± 3 -hour data window centered on the analysis times (0000, 0600, 1200, and 1800 UTC). Following Bloom et al. (1996), an analysis tendency (OI “After Analysis” minus GCM “First Guess” over 6-hours) is computed on the GCM sigma surfaces and used as a constant model forcing during the assimilation. With this method the model is not re-initialized at the analysis intervals, and the entire assimilation may be viewed as a continuous integration of the GCM in which the analysis increments act as another of the physical parameterizations. In fact, the interface between the GCM and the DAS is programmed in just this way.

3 Comparison of GEOS-1 Simulation and Analysis

In this section we analyze the climatology of the GEOS-1 GCM. These results are from a five-year simulation that was run in parallel with the five-year reanalysis. Initial conditions were identical for the reanalysis and the simulation, being generated from the January 1, 1985 analysis from the European Center for Medium Range Weather Forecasts (ECMWF). January and February of 1985 were considered a spin-up period. The results presented in this section are for the five-year period March 1985 through February 1990. All results are derived from output which was accumulated four times daily from both the model simulations and the GEOS-1 DAS analysis.

Boundary conditions (which include orography, sea surface temperature, ground wetness, sea ice cover, and surface albedo) were also identical in the two runs. Sea surface temperature and sea ice cover were taken from yearly varying monthly mean AMIP data (Gates, 1992), and the yearly varying monthly mean soil moisture from the estimates of Schemm et al. (1992). Seasonally-varying climatological values of surface albedo were based on Posey and Clapp (1964). At every GCM time step, values of all time-varying boundary conditions were linearly interpolated between the prescribed monthly means. The surface orography was obtained by averaging the Navy 10 minute by 10 minute dataset supplied by the National Center for Atmospheric Research (NCAR). A Lanczos (1966) filter was applied to the orography in both dimensions, removing the smallest scales while inhibiting the occurrence of negative values caused by the Gibbs phenomenon. Resulting negative values were *not* filled.

3.1 The Zonal Mean Circulation

The simulation of the zonal mean flow suffers from many of the same failings as other GCMs. Figure 1 shows December-January-February (DJF) zonal-mean zonal wind for the simulation and for the analysis, as well as zonal wind and temperature differences (simulation – analysis). Figure 2 shows the same fields for June-July-August (JJA). The most notable errors in the zonal mean flow are the westerly biases in the middle and high latitudes, particularly above 200 mb, and the inability of the model to produce negative vertical shears at upper levels and close the tropospheric jets. This is associated with the usual “cold pole”

problem. Note that the largest westerly biases tend to be on the poleward flanks of the subtropical jets, rather than over the jet cores. In northern hemisphere DJF, for example, this results in an easterly bias at the jet core. Zonal wind errors tend to be less pronounced in both hemispheres during JJA, when the model actually closes the jet in the northern hemisphere; even in this case, however, the model has a cold pole and a strong westerly shear. We will return to these biases in sections 4 and 5, where we discuss the effects of the numerics and of including gravity wave drag on the zonal flow.

Below 500 mb, the wind errors follow more or less the same meridional pattern as in the upper levels, but with little vertical shear. By far the largest errors in low-level winds are the excessive midlatitude westerlies during DJF in the northern hemisphere. In the southern hemisphere the low-level wind also shows a westerly bias in midlatitudes and a definite easterly bias poleward of 60S. In the southern hemisphere, however, biases are much smaller than in the northern hemisphere and are fairly uniform around the year.

During JJA the zonal-mean flow tends to show double jets at midtropospheric levels in both hemispheres (30S and 50S; 45N and 70N). The model clearly reproduces this feature in the southern hemisphere, but it fails to capture the weak high latitude jet in the northern hemisphere, which is associated with a weak secondary maximum in the vertical shear.

The low latitude easterlies are well simulated. At low levels the model shows the monsoonal asymmetry of stronger trades in the winter hemisphere and weaker—actually slightly westerly during JJA—in the summer hemisphere. Aloft, the model properly simulates the stronger easterlies of the summer hemisphere and captures the asymmetry between JJA and DJF. During DJF it tends to produce a westerly bias near the equator, peaking just above 200mb.

The temperature biases shown in Figs. 1 and 2 reveal that the model atmosphere is too cold everywhere, except for the lower troposphere at high northern latitudes during JJA. As shown by Boer et al. (1992), who compared results from fourteen models, this general cold bias seems to be common to many GCMs. In addition to the cold pole bias known to occur in almost all models at upper levels, they identified a nearly universal tendency to produce a cold bias throughout the tropical troposphere. In our case, the tropical tropospheric bias is nearly 2°C and quite constant from the surface to about 250 mb. This is comparable in magnitude to the biases reported by Boer et al. (1992) and is also comparable to the bias obtained by Kanamitsu et al. (1990) with the National Meteorological Center Medium-Range Forecast model run at triangular truncation T40.

The simulated extratropical troposphere is also too cold in both hemispheres during DJF and in the southern hemisphere during JJA. Although these biases are not as uniform as the tropical biases, they are roughly equal in magnitude (1°C to 2°C), resulting in the weak vertical shears in the lower tropospheric wind biases noted earlier. From the temperature errors shown in Fig. 2, we see that the failure of the model to produce the weak maximum in the vertical shear at high northern latitudes during JJA is associated with a warm bias poleward of 70N, which reaches 3°C near the surface at the pole. This suggests a problem with the model's summertime surface energy balance over the Arctic.

Figure 3 depicts the zonal-mean meridional velocity. Since the analysis of the divergent component of the wind is strongly influenced by the model, we should be particularly suspicious of agreements in the mean meridional circulations simulated and analyzed by the same model. For this reason, we have also shown results from the ECMWF analysis averaged over the same period of March 1985 through February 1990. Both analyses are uninitialized. The winter Hadley cell during DJF seems to bear out our suspicion. In the simulation and the GEOS analysis, the upper branch reaches a speed of only 1.5 m sec^{-1} , while in the ECMWF analysis it is nearly twice as strong. It is hard to say whether the model is biasing the analysis and underestimating the strength of the Hadley cell, or if the ECMWF analysis overestimates it. However, results from the National Meteorological Center analysis (not shown) are in closer agreement to the ECMWF analysis, with a maximum wind speed of 2.5 m sec^{-1} . For the winter Hadley cell in JJA the GEOS and ECMWF analyses are in closer agreement, with GEOS having the stronger cell of the two. In this case the simulation produces a weaker cell than either analysis.

The southern hemisphere Ferrel cells during both seasons are considerably stronger in the simulation than in the analyses. The same is true of the northern hemisphere Ferrel cell during DJF, with a stronger and deeper upper branch and much stronger low level flow. The unrealistically strong Ferrel cells are related to the unrealistic transient eddy momentum fluxes, which we discuss in the next section.

Figures 4a,b depict the zonal mean specific humidity simulated for JJA and its difference from the analysis. Results are shown only below 300 mb, since no analysis is done above this level. Near the surface the simulation is systematically drier in the tropics and subtropics and wetter in middle and high latitudes. Away from the surface the situation is more complicated. In the northern hemisphere there is a maximum in the wet bias between 900 and 950 mb (presumably at or just above the top of the boundary layer) and extending from 15N to 60N. Just north of the equator, at the position of the ITCZ, the model produces a dry bias that extends throughout the troposphere. This and the upper tropospheric wet biases in the subtropics are probably associated with errors in the simulation of deep convection. Finally, the model shows another maximum in the wet bias in the lower troposphere over the Arctic. This is the one region where the simulated zonal mean temperature was warmer than the analysis. The model exhibits a similar dry bias at low levels in the tropics during DJF (not shown). The wet bias in the extratropics, however, is substantially less.

Since the model has a significant temperature bias in the lower troposphere, we wondered how much of the moisture bias could be explained by temperatures errors and how much involved changes in relative humidity. We separated these two effects crudely by computing the difference between the analyzed specific humidity and the humidity of air at the simulated temperature, but at the analyzed *relative* humidity. This is shown in Fig. 4d. The residual between this field and the total error in specific humidity may be thought of as the part of the bias due to relative humidity errors. This is shown in Fig. 4e. As we can see from these two figures, most of the wet biases can be accounted for by errors in relative humidity; only the wet bias over the Arctic is attributable to temperature errors. In the tropics and subtropics between 950mb and 700 mb, the two effects tend to compensate; but the dry biases very near the surface are dominated by the temperature contribution.

The simulation of relative humidity is shown in Fig. 4f. Note that these results extend to 20 mb. For comparison, we show in Fig. 4c a composite of observations. Below 300 mb we use values obtained from the analysis; above 100 mb, we form a relative humidity from the zonal mean specific humidity climatology estimated from the Stratospheric Aerosol and Gas Experiment (SAGE) data and the analyzed zonal mean temperatures; between 100 and 300 mb, we blend the two. Results in the troposphere confirm the model's tendency to produce too high relative humidity almost everywhere away from the surface. But these errors are small compared to those above 300 mb. In the stratosphere, the model produces a gross overestimate of the relative humidity, with a high and diffuse tropopause distribution. Specific humidities above the tropical tropopause are up to 10 times larger than in the SAGE data. Since humidity is not analyzed above 300 mb, the analysis (not shown) reflects the model's bias and shows almost identical overestimates of stratospheric humidity. Unfortunately, both the simulation and the analysis used these unrealistic humidities in the radiation calculation.

Finally, we note that, as with the mean meridional circulation, the model has a strong effect on the moisture analysis. By comparing the analyzed total precipitable water with that derived from the Special Sensor Microwave/Imager (SSM/I), Molod et al. (1996) find that the analysis itself has a dry bias in the tropics. This implies that the simulation probably has an even greater dry bias in this region than that suggested by Fig. 4. In the extra-tropics, however, the analysis is in closer agreement with the SSM/I values, and we can have more confidence that the differences presented in Fig. 4 are representative of the true bias in the simulation.

3.2 The Stationary Flow

The simulation of the upper tropospheric stationary flow is summarized in Fig. 5, which shows the 200 mb zonal wind and the 300 mb eddy height fields for DJF. The model does a particularly good job of simulating the zonal wind distribution over the tropics. Most of the detail in the two regions of tropical westerlies over the eastern Pacific and the Atlantic is correctly simulated, as are the easterly maxima over South America, the maritime continent, and equatorial Africa. In the simulation, tropical easterlies tend to be too weak over the central Indian Ocean and a bit too strong over Africa and the maritime continent, regions of strong convective activity.

In the extratropics, we see good agreement in the position of the North American and East Asian jets, and of the subtropical jet over Arabia and North Africa. A detailed examination, however, reveals that in the simulation the Atlantic jet extends too far east into western Europe. The core of the Pacific jet is somewhat weak, and is tilted slightly toward the north rather than the more zonal configuration found in the analysis. Although, as we saw earlier, there is a slight zonal mean easterly bias at 30N, most of the weakness in the East Asian and North American jets can be attributed to a weakness in the standing eddies. The simulated Asian low at 300 mb is half the strength of the observed and the North American trough is also weak and displaced eastward and equatorward. We have not tried to analyze

the source of these deficiencies, but given the biases shown earlier in the zonal mean flow, particularly for northern hemisphere winter, such errors in the upper-level standing wave pattern are not surprising.

Figure 6 depicts the DJF and JJA seasonal means of the sea-level pressure. We focus first on the very poor simulation of the northern hemisphere pattern during DJF. The maximum zonal mean pressure at 30N is too high by about 5 mb, while pressures at the North Pole are 35 mb too low. This large error in the mean gradient, which is associated with the low-level midlatitude westerly biases shown in Fig. 1, results in a very zonal pattern that masks the presence of stationary features, such as the Aleutian and Icelandic lows. The same, but much weaker, tendency to produce an unrealistically low pressure at high latitudes and westerly biases in midlatitudes occurs during both seasons in the southern hemisphere. The northern hemisphere during JJA does not suffer from this problem, as we saw in Fig. 2. Setting aside this zonally symmetric bias, we note that most of the observed features are present, though somewhat distorted, in the simulation. This is seen more clearly in Fig. 7, which shows only the eddy part of the sea-level pressure during DJF. The Aleutian low is too weak and positioned too far west, and the Icelandic low has an unrealistic extension over northern Europe.

3.3 Eddy Statistics

In this section we present the zonal-mean transient and stationary eddy statistics. We will restrict our attention to the eddy kinetic energy and to meridional fluxes of westerly momentum, heat, and moisture. Transient eddy quantities are defined as products of the departures from the sixty individual monthly means in the five-year period being analyzed. In computing the transients, the zonal mean is not removed. The stationary quantities are products of the departures from the zonal mean of the individual monthly means. Once these monthly-mean statistics are obtained for each of the sixty months, they are averaged to produce seasonal (DJF and JJA) and annual means. To summarize the main features of the eddy quantities, we have chosen to present only the mass-weighted vertical means for the two seasons (Figs. 8 and 11) and to show only the annual means of their zonal cross sections (Figs. 9, 10, and 12).

The poleward momentum flux by transient eddies is overestimated for both seasons in both hemispheres. The situation is worst in the northern hemisphere during DJF, when the maximum in the poleward flux is nearly twice that of the analysis. This overestimate, together with a slight poleward shift of the maximum, results in a spurious deceleration of the westerly flow equatorward of roughly 40N and a spurious acceleration poleward of 40N. This is consistent with the zonal flow biases obtained during this season (Fig. 1). The meridional cross sections of the annual mean momentum flux (Fig. 9) show that the model does a good job of simulating the vertical structure with a maximum flux between 200 mb and 300 mb. The momentum flux by stationary waves (Fig. 10) is significant only in the northern hemisphere during DJF. The model does a reasonable job of simulating the maximum poleward stationary flux in midlatitudes—though it too is somewhat exaggerated—but fails

completely in simulating the equatorward flux north of about 50N.

The errors found in the northern hemisphere DJF simulation of total eddy momentum flux are qualitatively similar to those reported by Tibaldi et al. (1990) for the ECMWF model at spectral resolutions comparable to and higher than our grid resolution.¹ They also found large errors in the transports due to synoptic scale waves and to long planetary waves, and these are similar to the errors we obtain for transient and stationary waves: too much poleward flux by transients in midlatitudes, not enough equatorward flux by stationary waves in high northern latitudes.

Errors in the transient kinetic energy follow closely those in the momentum fluxes (cf. Figs. 8 and 9). The kinetic energy is slightly overestimated in the southern hemisphere during both seasons and very significantly overestimated (about 20%) in the northern hemisphere during DJF. This result is somewhat surprising since at this resolution we would anticipate the horizontal diffusion to play an important role in the kinetic energy budget and for the kinetic energy to be well below its convergent value. This is illustrated in the work of Tibaldi et al. just cited. Even though they obtain overestimates of the momentum flux similar to ours, their simulated eddy kinetic energy is everywhere less than the observed, even at higher (T106) horizontal resolution. The fact that our error in transient kinetic energy is an overestimate (even with the excessive dissipation associated with the low resolution we are using) suggests that it is linked to an excessive generation associated with errors in the zonal mean state.

The notion that the simulation has overly vigorous transients is reinforced by the heat and moisture fluxes shown in Fig. 11, 12, and 13. Midlatitude transient fluxes are consistently overestimated. The biggest errors are in the northern hemisphere during DJF, where transient heat fluxes reach twice the analyzed values. In this case, however, the stationary transport is nearly half that analyzed, producing almost complete compensation in the total heat flux. Interestingly, errors in moisture fluxes are significantly smaller than in heat flux. This is partly due to the fact that they peak at a lower latitude, where the simulation of the transients appears to be better. Moisture fluxes due to the stationary flow are also very well simulated during both seasons.

4 Resolution and Order-of-Accuracy Studies

In this section we analyze the sensitivity of the GEOS GCM climatology to resolution and order-of-accuracy. For this study, four separate experiments were performed and compared with the GEOS-1 simulation (referred to as the “Control” or H22) and GEOS-1 DAS analysis described in section 3.

In the first of these experiments, we simply run the second-order GEOS-1 model at the lower resolution of $4^\circ \times 5^\circ$. We will refer to this version as L22. We again note that this

¹We assume the dynamical behavior of T63 to be comparable to that of a 2 degree grid point model (Held and Suarez 1994).

Table 2: Sensitivity Experiments Summary

Experiment	Resolution	Vorticity Advection	θ and q Advection
Control(H22)	2x2.5	2nd-Order	2nd-Order
L22	4x5	2nd-Order	2nd-Order
L42	4x5	4th-Order	2nd-Order
L44	4x5	4th-Order	4th-Order
H44	2x2.5	4th-Order	4th-Order

was the model and resolution used for the DAO’s participation in AMIP. In the second simulation, we keep the low resolution but increase the order-of-accuracy by using a fourth-order scheme in the horizontal differencing of the momentum equation (L42). This was the finite-difference scheme used in the intercomparison of dynamical cores presented by Held and Suarez (1994). For the third simulation, we add to the preceding case a fourth-order scheme for the horizontal advection of potential temperature and moisture (L44). The fourth simulation repeats the last case but at the higher ($2^\circ \times 2.5^\circ$) resolution (H44). The experiments are summarized in Table 2.

The higher-order momentum scheme is a fourth-order version of the Sadourny scheme. This scheme was derived in Suarez and Takacs (1995). A brief discussion of the scheme and the final form of the finite-difference equations are presented here in the Appendix. The fourth-order horizontal advection scheme is the same as the scheme used in the UCLA GCM (Arakawa, personal communication).

Like the Control, all experiments were initialized from the January 1, 1985 ECMWF analysis, and were then run for a period of 26 months. We analyzed the last two years of these runs.

4.1 The Zonal Mean Circulation

We begin our analysis by examining the effects of resolution and order-of-accuracy on the annual mean climatology of zonal wind and temperature. We will focus our attention on two aspects of these simulations; 1) how the low-resolution, low order-of-accuracy simulation compares with the higher resolution and/or higher order-of-accuracy runs, and 2) how the model simulations compare with the GEOS-1 DAS analysis. Figure 14 shows the two-year average of the annual and zonal mean wind in the southern hemisphere at various pressure levels for the Control run, for experiments L22 through H44, and for the GEOS-1 DAS. It is evident that L22 exhibits a behavior which is distinctly different from that of the other experiments. For example, at 200 mb L22 has a narrowed jet with a single maximum that is shifted toward the equator to about 35°S . The L42 experiment, which adds fourth-order accuracy to the advection of vorticity, accurately maintains the breadth of the jet, while

L44 captures the double-jet structure that was simulated in the Control run and which is evident in the analysis. All simulations, however, produced stronger jets than the analysis. It is evident from these results that as order-of-accuracy and/or resolution are increased, the climatology of the southern hemisphere zonal wind is systematically converging to profiles which are similar to that of the analysis, but higher in magnitude. Note that near the surface, at 950 mb, all simulations except that of the second-order, low-resolution run had stronger surface winds than the DAS.

Figure 15 shows the two-year averaged annual and zonal mean wind for the northern hemisphere. Here we see a somewhat different result than in the southern hemisphere. At all levels, as order-of-accuracy and/or resolution are increased, the climatology of the northern hemisphere zonal wind moves systematically further, in both shape and strength, from that of the analysis. In this case, the low-resolution ($4^\circ \times 5^\circ$) run is the closest to the analysis. On the other hand, if we restrict our attention to the simulations and compare only *model* generated results, we see that the low-resolution fourth-order simulations, L24 and L44, are much closer to the higher resolution Control simulation (H22).

This large difference between the low order-of-accuracy $4^\circ \times 5^\circ$ and $2^\circ \times 2.5^\circ$ climatologies is consistent with resolution comparisons described by other authors. Boville's (1991) analysis of NCAR's CCM1, as well as results from Williamson et al. (1994) of NCAR's CCM2, showed that the climatology produced using a triangular truncation of T21 was significantly different from the climatologies produced using T42 or higher. This is also consistent with the results described by Tibaldi et al. (1990) and Boyle (1993) in analyzing the ECMWF model. The tendency of models to produce unrealistically strong zonal winds as resolution is increased has also been recognized for some time. This has been ascribed to deficiencies in modeling the drag exerted by orography on the zonal mean flow (e.g., Wallace et al. 1983, Palmer et al. 1986). At low resolution, unrealistically weak momentum transports compensate for orographic errors, leading to more realistic (weaker) zonal winds. We note that, in our case, unrealistically strong zonal surface and upper-level winds are observed even at low resolution when we increase the accuracy of vorticity advection (L42). While we would not expect orographic effects to play a major role on our errors in the southern hemisphere, their effects in the northern hemisphere may be quite substantial. We will return to this point and explore the source of these errors more closely in section 5.

Annual mean temperatures at 100 mb are shown in Fig. 16. We begin by noting that all simulations are colder than the corresponding analysis. In the tropics, this temperature bias is $\sim 5^\circ\text{C}$. At both poles, but particularly in the southern hemisphere, the cold pole bias is *worsened* as resolution and/or order-of-accuracy are increased. The low-resolution, low order-of-accuracy simulation, L22, is nearly 15°C warmer than the corresponding high-resolution Control run, while the low resolution, fourth-order simulation, L44, is practically identical to the Control run. It is interesting to note that most of the additional cold bias between L22 and L44 results from adding more accurate temperature advection (L42 \rightarrow L44), rather than just more accurate vorticity advection (L22 \rightarrow L42). While lower polar temperatures are consistent with the enhanced westerlies we found with increasing resolution and order-of-accuracy, it should also be noted that these results are contrary to those found by Mahlman and Umscheid (1987), in which temperatures above 50 mb were

shown to increase (toward observational values) with increasing resolution in the 40-level GFDL “SKYHI” GCM. Similarly, Chen and Bates (1995) found a reduction in the cold pole bias when the GEOS model was run with a semi-Lagrangian dynamical cores. However, in this case it is not clear whether the change in dynamical cores provided a real increase in accuracy.

Figure 17a shows the annual mean precipitable water differences between the Control run and the four experiments, while Fig. 17b shows the differences between the simulations and the GEOS-1 DAS analysis. It is clear from Fig. 17a that the low-resolution, low order-of-accuracy run (L22) has a distinctly different moisture climatology than the other simulations, with a significant moisture deficit in the tropics and excessive moisture at middle to high latitudes, as compared to the Control experiment (H22). Interestingly, just the use of fourth-order vorticity advection (L42) substantially removes this bias, and little additional improvement is seen when fourth-order advection of specific humidity is included (L44). We also see little impact when fourth-order accuracy is included at $2^\circ \times 2.5^\circ$ resolution (H44).

From Fig. 17b we see that all simulations exhibit a dry bias along the equator, and a moist bias on either side in the sub-tropics. In general, the simulations are producing a moist bias at middle to high latitudes in the northern hemisphere and a dry bias at middle to high latitudes in the southern hemisphere. Since L22 was wetter than the Control in the southern hemisphere, it is somewhat closer to the analysis in this region.

4.2 Eddy Statistics

Given the changes in the zonal mean wind, temperature, and specific humidity shown in the previous section, we may anticipate significant changes in the fluxes of momentum, heat, and moisture due to transient and stationary eddies. Figures 18-20 show the vertically integrated poleward fluxes of momentum, heat, and moisture from all experiments, as well as from the GEOS-1 DAS. Transient and stationary quantities are defined as in section 3.3. Turning our attention first to the momentum fluxes (Fig. 18), we see that in the southern hemisphere the analysis shows poleward flux equatorward of $\sim 60^\circ$ and equatorward flux at higher latitudes. All experiments but L22 reproduce this pattern. In L22 the transition between poleward and equatorward flux is displaced equatorward some 10° , as is the latitude of maximum convergence. The *magnitudes* of the fluxes, however, are best simulated by L22, while an exaggerated maximum in westerly momentum flux convergence is clearly evident in the other runs. In the northern hemisphere there is also a very systematic increase in the transient momentum flux with increasing order-of-accuracy and resolution. Comparing these results with the analysis, we see that this systematic increase takes us away from the observations, in spite of our increased accuracy. The analysis, in fact, most closely resembles the $4^\circ \times 5^\circ$ second-order result (L22).

Similar behavior can be seen in the northern hemisphere stationary fluxes. At high latitudes ($> 60^\circ\text{N}$), where the analysis shows an equatorward flux, there is a systematic tendency for

increasing poleward flux with increased accuracy. In general, all runs show a poleward bias in the stationary momentum flux outside the tropics. Since the meridional component of the Eliassen-Palm flux is the negative of the meridional momentum flux, this implies too much equatorward propagation of stationary waves — a bias which is probably related to errors in the zonal mean flow.

Figure 19 shows the sensitivity of the vertically integrated heat flux to resolution and order-of-accuracy. All model runs produce excessive transient heat fluxes in both hemispheres. In the southern hemisphere the position of the maximum transient flux improves somewhat with increasing accuracy and/or resolution. We see a similar result for the stationary flux in the southern hemisphere, with the magnitude also improving with increased order-of-accuracy and resolution. In the northern hemisphere the systematic increase in the poleward heat flux by transient eddies is partially compensated by a systematic decrease in the flux by the stationary flow with increasing order-of-accuracy and resolution. The analyzed flux obtained from the GEOS-1 DAS, however, more closely resembles the low-resolution, low order-of-accuracy result, with weaker flux from the transient flow and greater flux from the stationary flow. It is also interesting to note that improved accuracy of advection in the momentum equation (L22 \rightarrow L42) produces changes in the heat fluxes as great as those from improved accuracy of advection in the thermodynamic equation (L42 \rightarrow L44). This is in contrast to the behavior of the momentum fluxes, which were mostly sensitive to the formulation of momentum advection itself.

Finally, Fig. 20 shows the sensitivity of the vertically integrated moisture flux to resolution and order-of-accuracy. Interestingly, we see that contrary to the behavior of the transient momentum and heat fluxes, which *increased* with increasing accuracy and resolution, the transient flux of moisture *decreases* with increased accuracy and resolution. Also, increasing the accuracy has a significant impact on the moisture fluxes even at high resolution (H22 \rightarrow H44), whereas the heat and momentum fluxes were not very affected by order-of-accuracy at the higher resolution. This points out the care that must be taken in advecting water vapor, even in the horizontal, and suggests that this aspect should be improved in future versions of the model. It is encouraging that in the southern hemisphere, where model biases can easily affect the analysis, the transient flux from the fourth-order, $2^\circ \times 2.5^\circ$ resolution simulation (H44) is closer to the analysis than to the simulation produced from the model used in the GEOS-1 DAS (H22). In the northern hemisphere mid-latitudes (poleward of 40°N) there is a systematic decrease in the stationary moisture flux with increasing order-of-accuracy and resolution. This decrease, however, moves the simulation away from the analysis, with L22 again appearing to be the most realistic.

We have seen that several of the model biases presented in section 3 (such as the cold pole biases and the associated errors in vertical shear, the westerly bias in surface winds, and the excessive transient fluxes of heat and momentum) are not simply a result of inadequate accuracy in the discretization of the hydrodynamics. Rather, we have shown that in the northern hemisphere increasing the accuracy of the hydrodynamics has consistently produced zonal climatologies of wind, temperature, and meridional fluxes of heat and momentum which are further from the analysis. We will show in the following section that these biases are closely linked to the lack of sufficient upper-level drag associated with sub

grid-scale orographic gravity waves, and the lack of a sufficiently resolved stratosphere.

5 The Effects of Gravity Wave Drag

As shown in the preceding sections, the GEOS GCM suffers from several egregious errors which manifest themselves during the northern hemisphere winter season as cold biases at both poles and westerly biases in both jets, a severe zonality of the sea-level pressure and weak 300 mb eddy heights, enhanced transient fluxes, and weakened stationary fluxes in the northern hemisphere. Similar errors have been encountered by other authors (for example, Palmer et al. 1986, McFarlane 1987, and Boer and Lazare 1988) and, as mentioned earlier, have been ascribed to deficiencies in modeling the drag exerted by orography on the zonal mean flow. Typical of these studies is that the poleward transport of westerly momentum by transient eddies systematically increases when horizontal resolution is increased. These increases in the momentum transport must be balanced by changes in the mountain torque and/or increases in the surface frictional drag, thus requiring an increase in surface zonal wind. While most of these studies have found these errors at resolutions equivalent to $2^\circ \times 2.5^\circ$ resolution or higher, we have shown that in the GEOS model they occur even at low resolution when fourth-order accuracy is used. Further insight into the source of these errors may be gained by examining the simulated and analyzed angular momentum budgets. We will focus our attention first on the GEOS-1 GCM simulation (H22) and the GEOS-1 analysis.

The tendency of the vertically integrated and zonally averaged relative angular momentum may be expressed as

$$\begin{aligned} \frac{\partial}{\partial t} \int_0^1 [(\pi M_r)] \frac{d\sigma}{g} = & - \int_0^1 \frac{1}{a \cos \phi} \frac{\partial}{\partial \phi} [\pi v M_r] \cos \phi \frac{d\sigma}{g} + \int_0^1 f [\pi v] a \cos \phi \frac{d\sigma}{g} \\ & - \left[\frac{\pi}{g} \frac{\partial \Phi_s}{\partial \lambda} \right] - [\tau_s] a \cos \phi + \int_0^1 \frac{\partial}{\partial t} [\pi M_r]_A \frac{d\sigma}{g}, \end{aligned} \quad (1)$$

where square brackets denote a zonal mean,

$$M_r = ua \cos \phi$$

is the relative angular momentum,

$$\pi/g = (p_{surf} - p_{top})/g$$

is the mass of the model atmosphere per unit area, and all other notation is standard. The last term on the right-hand-side of Eq.(1) is the data-driven torque introduced by the analysis, and can be expanded as:

$$\int_0^1 \frac{\partial}{\partial t} [\pi M_r]_A \frac{d\sigma}{g} = \int_0^1 \left[\pi \left(\frac{\partial u}{\partial t} \right)_A \right] a \cos \phi \frac{d\sigma}{g} + \int_0^1 \left[u \left(\frac{\partial \pi}{\partial t} \right)_A \right] a \cos \phi \frac{d\sigma}{g}.$$

Here, we see that $\frac{\partial}{\partial t}(\pi M_r)_A$ is proportional to both the analysis increments of wind, $\left(\frac{\partial u}{\partial t}\right)_A$, and surface pressure, $\left(\frac{\partial \pi}{\partial t}\right)_A$, although this latter term is quite small. In the long-term mean, the time change of the relative momentum can be neglected in (1), as can the term proportional to f , since the mean mass flux across a latitude circle must be small. Thus, a balance will be obtained between the remaining terms predicted by the model (frictional torque, mountain torque, and momentum convergence) and the systematic error corrected by $\frac{\partial}{\partial t}(\pi M_r)_A$.

The solid lines in Fig. 21 show the momentum torques during the northern hemisphere winter season for the GEOS-1 analysis and the GEOS-1 simulation (H22). We see that the frictional torque due to surface stress is considerably larger in the simulation than in the analysis. This difference is associated with the stronger surface winds in the model simulation (see Fig. 1), which give rise to unrealistically large sources (in the tropics) and sinks (at mid-latitudes) of westerly momentum. Consistent with these increased sources and sinks is the increase in the meridional flux of westerly momentum described in section 3.3. Also evident in Fig. 21 is a complete lack of mountain torque poleward of 60N in the model simulation due to the severe zonality of the pressure field discussed in section 3.2. In this region the analysis shows the mountain torque balanced by an influx of easterly momentum, while in the simulation the atmosphere is bringing in westerly momentum — as in middle latitudes — which is balanced by an unrealistic frictional torque. Finally, we also show the residual between the frictional torque, the mountain torque, and the convergence of angular momentum. We see that in the simulation the residual is small, implying that there are no large spurious sources of momentum.² During the GEOS-1 DAS assimilation, however, the analysis had to introduce a significant easterly torque to remain close to the observational data. This analysis torque can be thought of as a correction to systematic errors in model numerics and/or parameterizations.

These results, together with those presented in sections 3 and 4, are suggestive of the need for a gravity wave drag parameterization in the GEOS GCM. Recently, Zhou et al. (1996) introduced a gravity wave drag parameterization into the Goddard Laboratory for Atmospheres (GLA) 4th-order GCM. This A-grid GCM was the predecessor of the C-grid GEOS-1 GCM and uses many similar algorithms and physical parameterizations. In their report, they found that many of the same biases found in the GEOS simulations (for example, the anomalous low pressure in the north polar region) were corrected in their model by gravity wave drag. Therefore, we decided to test their gravity wave drag parameterization in the GEOS system.

The gravity wave drag parameterization of Zhou et al. (1996) is a modified version of Vernekar et al. (1992), which was based on Alpert et al. (1988). In this version, the gravity wave stress at the surface is based on that derived by Pierrehumbert (1986) and is given by:

²This is gratifying because the numerical scheme we used does not guarantee angular momentum conservation.

$$|\vec{\tau}_{sfc}| = \frac{\rho U^3}{N \ell^*} \left(\frac{F_r^2}{1 + F_r^2} \right), \quad (2)$$

where $F_r = Nh/U$ is the Froude number, N is the *Brunt - Väisälä* frequency, U is the surface wind speed, h is the standard deviation of the sub-grid scale orography, and ℓ^* is the wavelength of the monochromatic gravity wave in the direction of the low-level wind. A modification introduced by Zhou et al. (1996) allows for the momentum flux to escape through the top of the model. For our study, h is set to the subgrid scale standard deviation of the Navy 10 minute by 10 minute topography, but is not allowed to exceed 400 m.

To test the gravity wave drag parameterization, we ran a 26-month simulation similar to those described in section 4 using the $4^\circ \times 5^\circ$ fourth-order model, L44. In section 4 we have shown that all of the model biases exhibited by the Control GEOS-1 GCM also exist and are well represented by the $4^\circ \times 5^\circ$ fourth-order model. Referring again to Fig. 21, the dashed lines depict the momentum torques obtained using the gravity wave drag parameterization. It is clear that L44 with gravity wave drag simulates very well the surface stress, mountain torque, and momentum convergence depicted by the GEOS DAS analysis. Moreover, the residual torque from this run (which is the torque introduced by the gravity wave drag parameterization) is very similar to the torque introduced by the analysis increments. This is a good indication that the systematic errors corrected by the assimilation resulted from the absence of gravity wave drag in the GEOS-1 model.

The effects of gravity wave drag on the momentum budget are seen more clearly in Fig. 22, which shows the differences in torques obtained with and without gravity wave drag, for northern hemisphere DJF. We see that gravity wave drag exerts an easterly torque between 20°N and 50°N and weak westerly torques at low and high latitudes. We might expect this to be balanced simply by a decrease in the frictional drag and mountain torques associated with decreased surface winds. But this is not at all the case. Changes in mountain torque are very small and changes in frictional drag are distributed very differently from the gravity wave drag. In fact, the frictional torque changes sign around 40°N — almost exactly at the latitude of maximum gravity wave drag, and the two are in the same direction equatorward of this latitude to 20°N . The outstanding result in Fig. 22 is the large change in the momentum transports. Equatorward of 45°N anomalous westerly convergence balances the gravity wave drag and frictional drag. At higher latitudes the mean balance is between the change in momentum transport and surface friction, with the gravity wave drag again being in the same direction as the frictional torque.

These changes in the fluxes can be seen more dramatically in Fig. 23, where we show the vertically integrated annual mean eddy fluxes of momentum and heat by the transient and stationary flow from the analysis, as well as from L44 with and without gravity wave drag. As shown in section 3.3, without gravity wave drag the flux of momentum and heat by transient eddies is much too strong. In the northern hemisphere the heat flux by the stationary flow is much too weak, while the momentum flux by the stationary flow lacks the equatorward component at high latitudes. With the inclusion of gravity wave drag, however, all of these fluxes are substantially improved. The transient wave statistics for momentum

and heat are practically identical to those of the analysis in the northern hemisphere. In addition, the heat flux due to the stationary flow has dramatically increased to a magnitude comparable to that from the analysis, while a significant equatorward component has emerged at high latitudes for the momentum flux by the stationary eddies.

As a result of these improvements in the fluxes of momentum and heat, the patterns of mean sea-level pressure and 300 mb eddy heights have also dramatically improved, as shown for DJF in Fig. 24. For ease of comparison, we have repeated the results from the GEOS-1 DAS. Most of the problems evident in Figs. 5 and 6 have been eliminated by the inclusion of gravity wave drag. The extreme low pressures and zonality in the northern hemisphere have been removed, while the positions of the Aleutian and Icelandic lows are substantially improved. It can also be seen that the strength of the 300 mb standing eddies have increased, while their positions are more accurately simulated.

Associated with these improvements in the mean sea-level pressure and 300 mb eddy heights, we also see improvements in the zonal mean wind structure and a reduction of the cold pole bias, shown in Fig. 25 for DJF. The panels on the left show results from the simulation using L44 with gravity wave drag. As compared to Fig. 1, we see that the jets are closed in both hemispheres; with substantial asymmetry in the jet maxima. The -22°C bias found in the H22 simulation in the northern hemisphere has been substantially reduced (-4° to -6°C). The -32°C bias found in H22 in the southern hemisphere has been moderated (-24°C), but its pattern has remained substantially intact.

While gravity wave drag has dramatically reduced the cold-pole bias, it is clear that there still remain significant errors at high latitudes, particularly in the southern hemisphere. Boville and Cheng (1988) and Tsuyuki (1994) have reported reductions in the cold-pole bias as a result of increased vertical resolution and better representation of the stratospheric circulation. Boville and Cheng compare two perpetual January simulations, one using 15 levels with a rigid lid at 10 mb and the other using 26 levels extending to 0.1 mb. Results showed a 20°C warming at 100 mb in the high resolution experiment. To test whether some of our remaining biases are due to our low vertical resolution and extent, we ran the L44 model with 46 levels (about 35 below 10 mb) and the top at 0.1 mb. This is the vertical resolution which was used for the DAO's participation in the ASHOE field mission. The panels on the right of Fig. 25 show DJF results from a two-year simulation. We see that increasing the vertical resolution and extent has further reduced the cold-pole bias, with the northern hemisphere actually becoming warmer than the analysis. While results from both the gravity wave drag parameterization and the stratospheric GCM are very preliminary, it is clear that they will produce a marked improvement in the model provided first guess to the GEOS DAS, and a substantial reduction in the systematic biases currently found in the analysis increments.

6 Summary

In this report we have analyzed the GEOS-1 GCM climatology from a five-year simulation, and compared it to the climatology of the five-year GEOS-1 DAS reanalysis for the period from March, 1985 through February, 1990. Due to the wide dissemination of the GEOS-1 DAS products to the scientific community, it is important that the behavior of the GCM used to produce them be thoroughly analyzed and documented. The behavior of physical processes in the model such as moist convection, radiative heating, surface fluxes, and the hydrological cycle is the focus of Molod et al. (1996). In this paper we concentrated on the behavior of the model's circulation statistics, with an emphasis on those biases in the simulated climate that may affect the analysis through systematic errors in the model provided first guess. In addition, the impact of several developments currently underway for future versions of the GEOS system have been explored.

In general the GEOS-1 GCM captures the main features of the general circulation. A detailed analysis of the GEOS-1 GCM's climatology of primary fields (wind, temperature, and specific humidity), however, has revealed significant systematic biases when compared with the GEOS-1 DAS analysis. The GEOS-1 GCM fails to accurately simulate the position and strength of the northern hemisphere winter Icelandic and Aleutian lows, and shows the increased zonality characteristic of models without a gravity-wave drag parameterization (Fig. 6). The model also exhibits a strong westerly bias in vertical shears and a significant cold bias at both poles (Figs. 1 and 2). Also typical of many other GCMs (cf. Boer et al. 1992), the model produces a cold bias throughout the tropical troposphere ($\sim 2^\circ\text{C}$). The model's distribution of moisture shows a significant dry bias in the tropics and subtropics at lower levels and a wet bias at middle and high latitudes (Fig. 4). Above 300 mb the model produces a gross overestimate of the relative humidity when compared to SAGE data. The low level dryness in the tropics was shown to be correlated primarily with the model's cold bias throughout the lower troposphere, whereas the middle and high latitude wet bias was associated with errors in relative humidity.

The second moments (horizontal momentum, heat, and moisture fluxes) also show several model biases and inaccuracies (Figs. 8 and 11). The GEOS-1 GCM consistently overestimates the meridional flux of westerly momentum and heat due to the transient eddies. In addition, in the northern hemisphere during DJF the flux of heat due to the stationary eddies is considerably weaker than observed and the stationary momentum flux is of the wrong sign at high latitudes.

In the second part of this report, we focused on the sensitivity of the GEOS GCM to resolution and order-of-accuracy. While the advantages of higher-order accuracy for passive tracer advection are readily apparent, the effect of higher-order accuracy on a GCM's climatology is not as obvious. We have shown that increasing the resolution and/or the order-of-accuracy in the GEOS GCM has a very significant impact on the zonal mean flow and on the second-moment statistics. In general, the climatology produced in the second-order, low resolution ($4^\circ \times 5^\circ$) experiment is significantly different from all other model generated climatologies (fourth-order, low resolution as well as second- and fourth-order,

high resolution ($2^\circ \times 2.5^\circ$)). In the southern hemisphere, the low-order, low-resolution simulation shows a marked equatorward shift of the zonal jet and large biases in momentum, heat, and moisture fluxes when compared to the higher resolution run (Figs. 14, 18, 19, and 20). Most of these biases appear to be related to the simulation of the transient eddies, with increased accuracy enhancing transient fluxes of heat and momentum and decreasing fluxes of moisture. In this region, where the total fluxes are dominated by the transient contribution, the higher-order and higher-resolution experiments are usually in closer agreement with the GEOS-1 DAS analysis.

In the northern hemisphere, where the role of fluxes due to the stationary eddies is significant, the zonal mean flow and heat and momentum fluxes tend systematically away from the GEOS-1 DAS analysis as accuracy and resolution are increased (Figs. 15, 18, 19, and 20). When comparing only *model* generated results, however, it was shown that the low-resolution, fourth-order simulations were much closer to the higher resolution Control simulation. Increasing the order-of-accuracy clearly improves the dynamical aspects of the simulations (in the sense that they are closer to the higher resolution results), even though these more accurate runs are further from the GEOS-1 DAS analysis. These results are consistent with the suggestion of Palmer et al. (1986) that increasing resolution and/or order-of-accuracy removes a cancellation of errors between the hydrodynamics and sub grid-scale parameterizations that occurs at low resolution and low order-of-accuracy.

We conclude this study by examining the impact of gravity wave drag on the climatology produced by the GEOS GCM. An examination of the angular momentum budgets from the GEOS-1 GCM and the five-year GEOS-1 DAS reanalysis for DJF shows the need for an easterly torque at mid-latitudes in the northern hemisphere to reduce the westerly bias (Fig. 21). This easterly torque is similar to that produced by gravity wave drag parameterizations currently used in many models. Experiments using the gravity wave drag parameterization of Zhou et al. (1996) yielded significant and beneficial impacts on both the time-mean flow and the transient statistics of the GEOS-1 GCM climatology, and have eliminated most of the worst biases in the GEOS-1 GCM simulation. An examination of the angular momentum budget from this run indicates that the resulting gravity wave torque is similar to the data-driven torque introduced by the GEOS-1 DAS analysis which was performed without gravity wave drag. It was shown that the inclusion of gravity wave drag results in large changes in both the mean flow and in eddy fluxes (Figs. 23 and 24). The result is a more accurate simulation of surface stress (through a reduction in the surface wind strength), of mountain torque (through a redistribution of mean sea-level pressure), and of momentum convergence (through a reduction in the flux of westerly momentum by transient flow eddies).

Acknowledgements This work was supported by the EOS Interdisciplinary Science Program and by the NASA Research and Applications Program. Computer resources and funding were provided by the EOS Project through the Scientific Computational Facility of the Data Assimilation Office.

Appendix

Fourth-Order Scheme for the Shallow Water Equations

In this section we present a new fourth-order enstrophy-conserving differencing of the momentum equation. To simplify the presentation, we apply the scheme to the shallow water equations in Cartesian coordinates, but its extension to the three-dimensional primitive equations on the sphere is straightforward.

A detailed derivation of the scheme is presented in Suarez and Takacs (1995). For reasons outlined there, we consider this scheme a fourth-order version of the Sadourny scheme used by Burridge and Haseler (1977). The scheme is based on the Arakawa C-grid and conserves energy and potential enstrophy for non-divergent flow. Also, it is fourth-order only in the sense that it reduces to the fourth-order Arakawa (1966) Jacobian for non-divergent flow. It thus provides fourth-order accuracy only in the advection of a second-order vorticity by the non-divergent part of the flow.

Following Sadourny (1975) and Arakawa and Lamb (1981), we begin by writing the shallow water equations for the two wind components (u,v) , and the fluid depth, h , in “vector-invariant” form as:

$$\begin{aligned}\frac{\partial u}{\partial t} &= -\eta h v - \frac{\partial}{\partial x} [\Phi + K] , \\ \frac{\partial v}{\partial t} &= \eta h u - \frac{\partial}{\partial y} [\Phi + K] , \\ \frac{\partial h}{\partial t} &= - \left[\frac{\partial h u}{\partial x} + \frac{\partial h v}{\partial y} \right] ,\end{aligned}$$

where

$$\eta = \frac{(f + \zeta)}{h}$$

is the potential vorticity, f is the Coriolis parameter, ζ is the relative vorticity,

$$\zeta = \frac{\partial v}{\partial x} - \frac{\partial u}{\partial y},$$

K is the kinetic energy per unit mass,

$$K = \frac{1}{2} [u^2 + v^2],$$

$$\Phi = g (h + h_s),$$

g is the acceleration of gravity, and h_s is the height of the surface topography.

Following Arakawa and Lamb (1981), we discretize the shallow water system as:

$$\begin{aligned}
\left(\frac{\partial u}{\partial t}\right)_{i+\frac{1}{2},j} &= \frac{1}{\Delta x} \left[\alpha_{i+\frac{1}{2},j} v_{i+1,j+\frac{1}{2}}^* + \beta_{i+\frac{1}{2},j} v_{i,j+\frac{1}{2}}^* + \gamma_{i+\frac{1}{2},j} v_{i,j-\frac{1}{2}}^* + \delta_{i+\frac{1}{2},j} v_{i+1,j-\frac{1}{2}}^* \right] \\
&- \frac{1}{\Delta x} \left[\nu_{i+\frac{1}{2},j+\frac{1}{2}} u_{i+\frac{1}{2},j+1}^* - \nu_{i+\frac{1}{2},j-\frac{1}{2}} u_{i+\frac{1}{2},j-1}^* \right] \\
&- \frac{1}{\Delta x} [(\Phi + K)_{i+1,j} - (\Phi + K)_{i,j}] , \\
\left(\frac{\partial v}{\partial t}\right)_{i,j+\frac{1}{2}} &= -\frac{1}{\Delta y} \left[\alpha_{i-\frac{1}{2},j} u_{i-\frac{1}{2},j}^* + \beta_{i+\frac{1}{2},j} u_{i+\frac{1}{2},j}^* + \gamma_{i+\frac{1}{2},j+1} u_{i+\frac{1}{2},j+1}^* + \delta_{i-\frac{1}{2},j+1} u_{i-\frac{1}{2},j+1}^* \right] \\
&- \frac{1}{\Delta y} \left[\mu_{i+\frac{1}{2},j+\frac{1}{2}} v_{i+1,j+\frac{1}{2}}^* - \mu_{i-\frac{1}{2},j+\frac{1}{2}} v_{i-1,j+\frac{1}{2}}^* \right] \\
&- \frac{1}{\Delta y} [(\Phi + K)_{i,j+1} - (\Phi + K)_{i,j}] , \\
\left(\frac{\partial h}{\partial t}\right)_{i,j} &= -\frac{1}{\Delta x \Delta y} \left[u_{i+\frac{1}{2},j}^* - u_{i-\frac{1}{2},j}^* + v_{i,j+\frac{1}{2}}^* - v_{i,j-\frac{1}{2}}^* \right] ,
\end{aligned}$$

where

$$\begin{aligned}
u_{i+\frac{1}{2},j}^* &= \bar{h}_{i+\frac{1}{2},j}^x u_{i+\frac{1}{2},j} \Delta y , \\
v_{i,j+\frac{1}{2}}^* &= \bar{h}_{i,j+\frac{1}{2}}^y v_{i,j+\frac{1}{2}} \Delta x , \\
\bar{h}_{i+\frac{1}{2},j}^x &= \frac{1}{2} (h_{i+1,j} + h_{i,j}) , \\
\bar{h}_{i,j+\frac{1}{2}}^y &= \frac{1}{2} (h_{i,j+1} + h_{i,j}) .
\end{aligned}$$

Refer to the stencil shown in Fig. 26 for the position of the various variables on the C-grid. We see that second-order differencing is used for the pressure gradient term and the continuity equation. The advection of potential vorticity is governed by the form of the parameters α , β , γ , δ , ν , and μ . We write these as:

$$(\alpha, \beta, \gamma, \delta)_{i+\frac{1}{2},j} = \epsilon (\alpha, \beta, \gamma, \delta)_{i+\frac{1}{2},j}^S + (1 - \epsilon) (\alpha, \beta, \gamma, \delta)_{i+\frac{1}{2},j}^N ,$$

where

$$\begin{aligned}
\alpha_{i+\frac{1}{2},j}^S &= \frac{1}{12} \left(\eta_{i+\frac{3}{2},j+\frac{1}{2}} + \eta_{i+\frac{1}{2},j+\frac{1}{2}} + \eta_{i+\frac{1}{2},j-\frac{1}{2}} \right) , \\
\beta_{i+\frac{1}{2},j}^S &= \frac{1}{12} \left(\eta_{i+\frac{1}{2},j+\frac{1}{2}} + \eta_{i-\frac{1}{2},j+\frac{1}{2}} + \eta_{i+\frac{1}{2},j-\frac{1}{2}} \right) ,
\end{aligned}$$

$$\gamma_{i+\frac{1}{2},j}^S = \frac{1}{12} \left(\eta_{i+\frac{1}{2},j+\frac{1}{2}} + \eta_{i+\frac{1}{2},j-\frac{1}{2}} + \eta_{i-\frac{1}{2},j-\frac{1}{2}} \right) ,$$

$$\delta_{i+\frac{1}{2},j}^S = \frac{1}{12} \left(\eta_{i+\frac{1}{2},j-\frac{1}{2}} + \eta_{i+\frac{1}{2},j+\frac{1}{2}} + \eta_{i+\frac{3}{2},j-\frac{1}{2}} \right) ,$$

$$\alpha_{i+\frac{1}{2},j}^N = \frac{1}{12} \left(\eta_{i+\frac{3}{2},j-\frac{1}{2}} + \eta_{i-\frac{1}{2},j+\frac{1}{2}} + \eta_{i+\frac{1}{2},j+\frac{3}{2}} \right) ,$$

$$\beta_{i+\frac{1}{2},j}^N = \frac{1}{12} \left(\eta_{i+\frac{1}{2},j+\frac{3}{2}} + \eta_{i+\frac{3}{2},j+\frac{1}{2}} + \eta_{i-\frac{1}{2},j-\frac{1}{2}} \right) ,$$

$$\gamma_{i+\frac{1}{2},j}^N = \frac{1}{12} \left(\eta_{i+\frac{1}{2},j-\frac{3}{2}} + \eta_{i+\frac{3}{2},j-\frac{1}{2}} + \eta_{i-\frac{1}{2},j+\frac{1}{2}} \right) ,$$

$$\delta_{i+\frac{1}{2},j}^N = \frac{1}{12} \left(\eta_{i-\frac{3}{2},j-\frac{1}{2}} + \eta_{i-\frac{1}{2},j-\frac{3}{2}} + \eta_{i+\frac{1}{2},j+\frac{1}{2}} \right) ,$$

and

$$\nu_{i+\frac{1}{2},j+\frac{1}{2}} = \frac{-(1-\epsilon)}{12} \left(\eta_{i+\frac{3}{2},j+\frac{1}{2}} - \eta_{i-\frac{1}{2},j+\frac{1}{2}} \right) ,$$

$$\mu_{i+\frac{1}{2},j+\frac{1}{2}} = \frac{-(1-\epsilon)}{12} \left(\eta_{i+\frac{1}{2},j-\frac{1}{2}} - \eta_{i+\frac{1}{2},j+\frac{3}{2}} \right) .$$

The second-order scheme used by Burridge and Haseler (1977) then corresponds to $\epsilon = 1$, and the new fourth-order scheme corresponds to $\epsilon = \frac{3}{2}$.

In the above equations, $\eta_{i+\frac{1}{2},j+\frac{1}{2}}$ is defined as

$$\eta_{i+\frac{1}{2},j+\frac{1}{2}} = \frac{\zeta_{i+\frac{1}{2},j+\frac{1}{2}} + f_{i+\frac{1}{2},j+\frac{1}{2}}}{\bar{h}_{i+\frac{1}{2},j+\frac{1}{2}}^{xy}} ,$$

where

$$\zeta_{i+\frac{1}{2},j+\frac{1}{2}} = \left(\frac{v_{i+1,j+\frac{1}{2}} - v_{i,j+\frac{1}{2}}}{\Delta x} \right) - \left(\frac{u_{i+\frac{1}{2},j+1} - u_{i+\frac{1}{2},j}}{\Delta y} \right) ,$$

and

$$\bar{h}_{i+\frac{1}{2},j+\frac{1}{2}}^{xy} = (h_{i+1,j+1} + h_{i,j+1} + h_{i,j} + h_{i+1,j})/4 .$$

The form of K for which the scheme conserves energy is:

$$K_{i,j} = \frac{1}{2} \left[\overline{u^2}_{i,j}^x + \overline{v^2}_{i,j}^y \right] ,$$

where

$$\overline{u^2}_{i,j}^x = \frac{1}{2} (u_{i+\frac{1}{2},j}^2 + u_{i-\frac{1}{2},j}^2) ,$$

$$\overline{v^2}_{i,j}^y = \frac{1}{2} (v_{i,j+\frac{1}{2}}^2 + v_{i,j-\frac{1}{2}}^2) .$$

Using this discrete form of the kinetic energy in the three-dimensional GCM will result in the computational instability discussed by Hollingsworth et al. (1983). A modification of this form which removes the instability is presented in Suarez and Takacs (1995).

Figure 1: Five year average of Northern Hemisphere winter zonal mean u-winds (m sec^{-1}) for the GEOS-1 GCM, the GEOS-1 DAS, and the u-wind and temperature difference (GCM-DAS).

Figure 2: Five year average of Northern Hemisphere summer zonal mean u-winds (m sec^{-1}) for the GEOS-1 GCM, the GEOS-1 DAS, and the u-wind and temperature difference (GCM-DAS).

Figure 3: Five year average of Northern Hemisphere winter and summer seasonal means of the zonal mean v-wind (m sec^{-1}) for the GEOS-1 GCM, the GEOS-1 DAS, and the uninitialized ECMWF analysis.

Figure 4: Five year average of JJA seasonal mean of the zonal mean a) specific humidity (g kg^{-1}) for the GEOS-1 GCM, b) specific humidity difference for the GCM-DAS, c) specific humidity difference due to temperature, d) specific humidity difference due to relative humidity, e) blended relative humidity using GEOS-1 DAS and SAGE, f) relative humidity from the GEOS-1 GCM.

Figure 5: Five year average of Northern Hemisphere winter seasonal means of the 200-mb u-wind (5 m sec^{-1}) contours, with negatives shaded) and 300-mb eddy-heights (60 m contours, with light shading $< 60 \text{ m}$ and dark shading $> 60 \text{ m}$) for the GEOS-1 GCM and the GEOS-1 DAS.

Figure 6: Five year average of Northern Hemisphere winter and summer seasonal means of Sea-Level Pressure (4 mb contours, with light shading < 988 mb and dark shading > 1020 mb) for the GEOS-1 GCM and the GEOS-1 DAS.

Figure 7: Five year average of DJF seasonal mean of the eddy Sea-Level Pressure (4 mb contours, with light shading < -4 mb and dark shading > 4 mb) for the GEOS-1 GCM and the GEOS-1 DAS.

Figure 8: Five year average of DJF and JJA seasonal means of the vertically integrated momentum flux ($\text{m}^2 \text{sec}^{-2}$), and kinetic energy ($\text{m}^2 \text{sec}^{-2}$), due to the transient and stationary flow for the GEOS-1 GCM and the GEOS-1 DAS.

Figure 9: Five year annual mean average of horizontal momentum flux ($\text{m}^2 \text{sec}^{-2}$) and kinetic energy ($\text{m}^2 \text{sec}^{-2}$) due to the transient flow for the GEOS-1 GCM and the GEOS-1 DAS.

Figure 10: Five year annual mean average of horizontal momentum flux ($\text{m}^2 \text{sec}^{-2}$) and kinetic energy ($\text{m}^2 \text{sec}^{-2}$) due to the stationary flow for the GEOS-1 GCM and the GEOS-1 DAS.

Figure 11: Five year average of DJF and JJA seasonal means of the vertically integrated heat ($\text{m sec}^{-1} \text{ deg}$), and moisture ($\text{m sec}^{-1} \text{ g kg}^{-1}$) fluxes due to the transient and stationary flow for the GEOS-1 GCM and the GEOS-1 DAS.

Figure 12: Five year annual mean average of meridional heat flux ($\text{m sec}^{-1} \text{ deg}$) due to the transient and stationary flow for the GEOS-1 GCM and the GEOS-1 DAS.

Figure 13: Five year annual mean average of meridional moisture flux ($\text{m sec}^{-1} \text{ g kg}^{-1}$) due to the transient and stationary flow for the GEOS-1 GCM and the GEOS-1 DAS.

Figure 14: Two year annual and zonal mean u-wind (m sec^{-1}) in the southern hemisphere for the Control (H22) run, experiments L22, L42, L44, H44, and the GEOS-1 DAS.

Figure 15: Two year annual and zonal mean u-wind (m sec^{-1}) in the northern hemisphere for the Control (H22) run, experiments L22, L42, L44, H44, and the GEOS-1 DAS.

Figure 16: Two year annual and zonal mean temperature (deg K) at 100 mb for the Control (H22) run, experiments L22, L42, L44, H44, and the GEOS-1 DAS.

Figure 17: Two year annual and zonal mean differences in precipitable water (g cm^{-2}) between a) experiments L22 through H44 and the Control (H22), and b) between L22 through H44, the Control (H22), and the GEOS-1 DAS.

Figure 18: Vertically integrated poleward momentum flux for the Control (H22) run, experiments L22, L42, L44, H44, and the GEOS-1 DAS, due to transient and stationary flow.

Figure 19: Vertically integrated poleward heat flux for the Control (H22) run, experiments L22, L42, L44, H44, and the GEOS-1 DAS, due to transient and stationary flow.

Figure 20: Vertically integrated poleward moisture flux for the Control (H22) run, experiments L22, L42, L44, H44, and the GEOS-1 DAS, due to transient and stationary flow.

Figure 21: Five year Northern Hemisphere winter seasonal averages of momentum torques for (a) the GEOS-1 DAS, and (b) the GEOS-1 GCM. Also shown is the two year DJF seasonal average for (c) the GEOS GCM with Gravity Wave Drag (L44 w/GWD). (Units are in 10^6 N m^{-1})

Figure 22: Two year DJF seasonal mean difference of momentum torques from the GEOS GCM with Gravity Wave Drag (L44 w/GWD) and the control (L44). (Units are in 10^6 N m^{-1})

Figure 23: Vertically integrated annual mean momentum and heat flux due to transient and stationary flow for the GEOS-1 DAS and experiments L44 and L44 w/GWD.

Figure 24: DJF Seasonal mean Sea-Level Pressure and 300 mb Eddy Heights from the GEOS GCM w/GWD and the GEOS-1 DAS.

Figure 25: Two year average of DJF zonal mean u-winds (m sec^{-1}) for the GEOS GCM w/GWD and the Stratospheric GEOS GCM w/GWD, and their temperature differences (GCM-DAS).

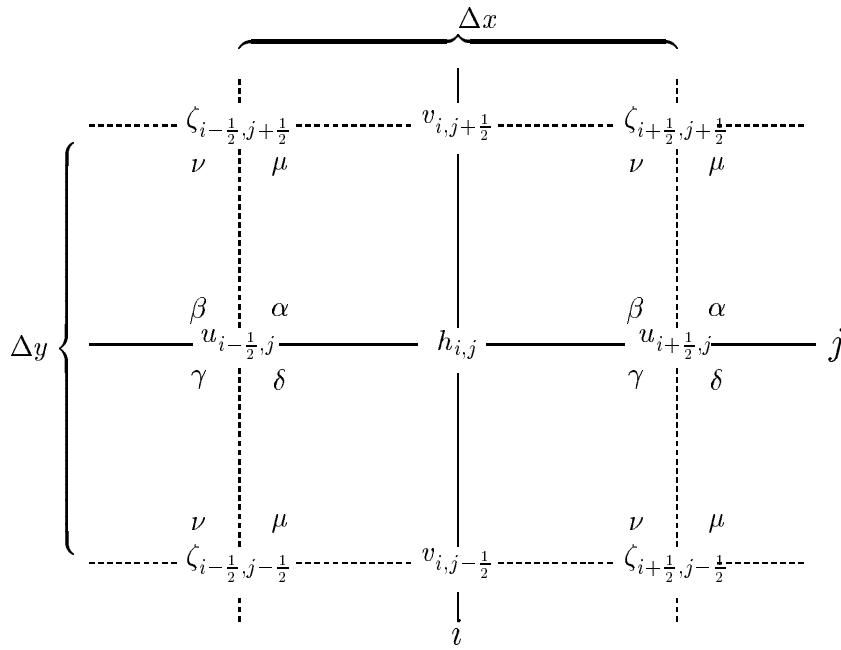


Figure 26: Stencil showing the position and indexing of the prognostic fields u , v , and h , together with the vorticity, ζ , and the scheme parameters α , β , γ , δ , ν , and μ .

References

- Alpert, J.C., M. Kanamitsu, P.M. Caplan, J.G. Sela, G.H. White and E. Kalnay, 1988: Mountain induced gravity wave drag parameterization in the NMC medium-range forecast model. *Proceedings of the Eighth Conference on Numerical Weather Prediction*, Baltimore, Maryland, February 22-26, 1988, 726-733.
- Arakawa, A., 1966: Computational design for long-term numerical integration of the equations of fluid motion: Two-dimensional incompressible flow. Part I. *J. Comput. Phys.*, **1**, 119-143.
- Arakawa, A. and V.R. Lamb, 1981: A potential enstrophy and energy conserving scheme for the shallow water equations. *Mon. Wea. Rev.*, **109**, 18-36.
- Arakawa, A. and M.J. Suarez, 1983: Vertical differencing of the primitive equations in sigma coordinates. *Mon. Wea. Rev.*, **111**, 34-45.
- Baker, W.E., S.C. Bloom, J.S. Woollen, M.S. Nester, E. Brin, T.W. Schlatter, and G.W. Branstator, 1987: Experiments with a Three-Dimensional Statistical Objective Analysis Scheme Using FGGE Data. *Mon. Wea. Rev.*, **115**, 272-296.
- Bloom, S.C., L.L. Takacs, and E. Brin, 1991: A scheme to incorporate analysis increments gradually in the GLA assimilation system. *Ninth Conf. on Numerical Weather Prediction*, Denver, CO, Amer. Meteor. Soc., 110-112.
- Bloom, S.C., L.L. Takacs, A.M. DaSilva, and D. Ledvina, 1996: Data Assimilation Using Incremental Analysis Updates. In press *Mon. Wea. Rev.*.
- Boer, G. J., K. Arpe, M. Blackburn, M. Déqué, W.L. Gates, T.L. Hart, H. Le Treut, I. Roeckner, D.A. Sheinin, I. Simmonds, R.N.B. Smith, T. Tokioka, R.T. Wetherald, and D. Williamson, 1992: Some Results From and Intercomparison of the Climates Simulated by 14 Atmospheric General Circulation Models, *J. Geophys. Res.*, **97**, 12771-12786.
- Boer, G. J., and M. Lazare, 1988: Some results concerning the effect of horizontal resolution and gravity-wave drag on simulated climate. *J. Climate*, **1**, 789-806.
- Boville, B. A., 1991: Sensitivity of simulated climate to model resolution. *J. Climate*, **4**, 469-485.
- Boville, B. A., and Xinhua Cheng, 1988: Upper Boundary Effects in a General Circulation Model. *J. Atmos. Sci.*, **45**, 2591-2606.
- Boyle, J. S., 1993: Sensitivity of Dynamical Quantities to Horizontal Resolution for a Climate Simulation Using the ECMWF (Cycle 33) Model. *J. Climate*, **6**, 796-815.
- Burridge, D.M. and J. Haseler, 1977: A model for medium range weather forecasting —

- adiabatic formulation, *Tech. Report. No. 4, European Center for Medium Range Weather Forecasts*, Brachnell, Berkshire, U.K., 46 pp.
- Chen, M., and J.R. Bates, 1995: Intercomparison of Climate Simulations from a Semi-Lagrangian and an Eulerian GCM. submitted to *J.Climate*.
- Gates, W. Lawrence, 1992: AMIP: The Atmospheric Model Intercomparison Project. *Bull. Am Met. Soc.*, **73**, 1962-1970
- Harshvardhan, R. Davies, D. A. Randall, and T. G. Corsetti, 1987: A fast radiation parameterization for atmospheric circulation models. *J. Geophys. Res.*, **92**, 1009-1016.
- Held, I.M. and M.J. Suarez, 1994: A proposal for the intercomparison of the dynamical cores of atmospheric general circulation models. *Bull. Am Met. Soc.*, **75**, 1825-1830.
- Helfand, H. M., and J. C. Labraga, 1988: Design of a non-singular level 2.5 second-order closure model for the prediction of atmospheric turbulence. *J. Atmos. Sci.*, **45**, 113-132.
- Hollingsworth, A., P. Källberg, V. Renner, and D.M. Burridge, 1983: An internal symmetric computational instability, *Quart. J. R. Met Soc.* , **109**, 417-428.
- Kalnay-Rivas, E., A. Bayliss and J. Storch, 1977: The 4th order GISS model of the global atmosphere. *Beitr. Phys. Atmos.*, **50**, 299-311.
- Kanamitsu, M., K.C. Mo, and E. Kalnay, 1990: Annual Cycle Integration of the NMC Medium-Range Forecasting (MRF) Model. *Mon. Wea. Rev.*, **118**, 2543-2567.
- Kreiss, H.O., and J. Olinger, 1972: Comparison of accurate methods for the integration of hyperbolic equations. *Tellus*, **24**, 199-215.
- Lanczos, C., 1966: *Discourse on Fourier Series*. Hafner Publishing, 255 pp.
- Mahlman, J. D., and L. J. Umscheid, 1987: Comprehensive modeling of the middle atmosphere: The influence of horizontal resolution. *Transport Processes in the Middle Atmosphere*, G. Visconti and R. Garcia, Eds, Reidel, 251-266.
- McFarlane, N. A., 1987: The effect of orographically excited gravity-wave drag on the general circulation of the lower stratosphere and troposphere. *J. Atmos. Sci.*, **44**, 1775-1800.
- Molod, A., Helfand, H. M., and L. L. Takacs, 1996: The Climatology of Parameterized Physical Processes in the GEOS-1 GCM and their Impact on the GEOS-1 Data Assimilation System. In press *J. Climate*.
- Moorthi, S., and M. J. Suarez, 1992: Relaxed Arakawa Schubert: A parameterization of moist convection for general circulation models. *Mon. Wea. Rev.*, **120**, 978-1002.
- Palmer, T. N., G. J. Shutts, and R. Swinbank, 1986: Alleviation of a systematic westerly bias in general circulation and numerical weather prediction models through an orographic gravity wave drag parameterization. *Quart. J. R. Met. Soc.*, **112**, 1001-1039.

- Pfaendtner, J., S. Bloom, D. Lamich, M. Seablom, M. Sienkiewicz, J. Stobie, and A. da Silva, 1995: Documentation of the Goddard Earth Observing System (GEOS) Data Assimilation System - Version 1, NASA Technical Memorandum 104606 Volume 4, Goddard Space Flight Center, Greenbelt, MD 20771, 58 pp. [also available from suarez@maxs.gsfc.nasa.gov].
- Pierrehumbert, R.T., 1986: An essay on the parameterization of orographic gravity-wave drag. *Proc. Seminar/Workshop on observation, theory and modeling of orographic effects*. 15-20 September, ECMWF, Shinfield Park, Reading, U.K., **1**, 251-282.
- Posey, J. W., and P. F. Clapp, 1964: Global distribution of normal surface albedo. *Geofis. Int.*, **4**, 33-48.
- Russel, G.L., K. Takano, and F. Abramopoulos, 1986: Comparison of Horizontal Difference Schemes for the Shallow Water Equations on a Sphere. *Collection of Papers Presented at the WMO/IUGG NWP Symposium*, Tokyo, 4-8 August, 1986.
- Schemm, J., S. Schubert, J. Terry, and S. Bloom, 1992: Estimates of monthly mean soil moisture for 1979-1989. NASA Technical Memorandum 104571, Goddard Space Flight Center, Greenbelt, MD 20771, 260 pp.
- Schubert, S.D., C.K. Park, C.Y. Wu, W. Higgins, Y. Kondratyeva, A. Molod, L. Takacs, M. Seablom, and R. Rood, 1995: A Multiyear Assimilation with the GEOS-1 System: Overview and Results, NASA Technical Memorandum 104606 Volume 6, Goddard Space Flight Center, Greenbelt, MD 20771, 207 pp. [also available from suarez@maxs.gsfc.nasa.gov].
- Schubert, S. D., J. Pfaendtner and R. Rood, 1993: An assimilated data set for Earth Science applications. *Bull. Am Met. Soc.*, **74**, 2331-2342.
- Suarez, M. J., and L. L. Takacs, 1995: Documentation of the Aries/GEOS Dynamical Core Version 2, NASA Technical Memorandum 104606 Volume 5, Goddard Space Flight Center, Greenbelt, MD 20771, 58 pp. [also available from suarez@maxs.gsfc.nasa.gov].
- Sud, Y. C., and A. Molod, 1988: The roles of dry convection, cloud-radiation feedback processes and the influence of recent improvements in the parameterization of convection in the GLA GCM. *Mon. Wea. Rev.*, **116**, 2366-2387.
- Takacs, L. L. , A. Molod, and T. Wang, 1994: Documentation of the Goddard Earth Observing System (GEOS) General Circulation Model-Version 1. NASA Technical Memorandum 104606 Volume 1, Goddard Space Flight Center, Greenbelt, MD 20771, 97 pp. [also available from suarez@maxs.gsfc.nasa.gov].
- Tibaldi, S., T. N. Palmer, C. Brankovic, and U. Cubasch, 1990: Extended-range predictions with ECMWF models: Influence of horizontal resolution on systematic error and forecast skill. *Quart. J. Roy. Meteor. Soc.*, **116**, 835-866.

- Tsuyuki, Tadashi, 1994: Impacts of Increased Vertical Resolution in the Stratosphere on Dynamical Extended-Range Forecasts. *J. Meteor. Soc. Japan*, **72**, 795-810.
- Vernekar, A.D., B. Kirtman, D. DeWitt and J. Zhou, 1992: Orographic gravity-wave drag effects on medium-range forecasts with a general circulation model. *Physical Processes in Atmospheric Models*. Edited by D.R. Sikka and S.S. Singh. Wiley Eastern Limited. 295-307.
- Wallace, J.M., S. Tibaldi, and A.J. Simmons, 1983: Reduction of systematic forecast errors in the ECMWF model through the introduction of an envelope orography. *Quart. J. Roy. Meteor. Soc.*, **109**, 683-717.
- Williamson, D.L., J.T. Kiehl, and J.J. Hack Cubasch, 1994: Climate Sensitivity of the NCAR Community Climate Model (CCM2) to Horizontal Resolution. submitted to *Climate Dynamics*.
- Zhou, J., Y.C. Sud, and K.-M. Lau, 1996: Impact of Orographically Induced Gravity Wave Drag in the GLA GCM. In press *Quart. J. Roy. Meteor. Soc.*.